

## Article

# Experimental Investigation and Modeling: Considerations of Simultaneous Surface Steel Droplets' Evaporation and Corrosion

Marius Ciprian Ilie<sup>1,2</sup>, Timur Vasile Chiș<sup>3</sup> , Ioana Maior<sup>4</sup>, Cristian Eugen Răducanu<sup>1,\*</sup>,  
Iuliana Mihaela Deleanu<sup>1</sup> , Tănase Dobre<sup>1,5,\*</sup> and Oana Cristina Pârvulescu<sup>1</sup> 

- <sup>1</sup> Chemical and Biochemical Engineering Department, National University of Science and Technology Politehnica Bucharest, 1-7 Gheorghe Polizu St., 011061 Bucharest, Romania; ciprian.ilie@totalenergies.com (M.C.I.); iuliana.deleanu@upb.ro (I.M.D.); oana.parvulescu@yahoo.com (O.C.P.)
- <sup>2</sup> TotalEnergies Marketing Romania SA, 4 Vasile Alecsandri St., 010639 Bucharest, Romania
- <sup>3</sup> Doctoral School Associate, Petroleum-Gas University of Ploiești, 39 Bucharest Blvd., 100680 Ploiesti, Romania; timur.chis@gmail.com
- <sup>4</sup> Inorganic Chemistry, Physical Chemistry and Electrochemistry Department, National University of Science and Technology Politehnica Bucharest, 1-7 Gheorghe Polizu St., 011061 Bucharest, Romania; ioana.maior@upb.ro
- <sup>5</sup> Technical Sciences Academy of Romania, 26 Dacia Boulevard, 030167 Bucharest, Romania
- \* Correspondence: cristianrdcn1@yahoo.com (C.E.R.); tghdobre@gmail.com (T.D.)

**Abstract:** The present work focuses on the problem of steel surface corrosion as a kinetic expression when water droplets are repeatedly deposited and evaporated on/from its surface. This process, together with the rainwater film corrosion process, belongs to the theoretical foundations of the problem of atmospheric corrosion. It was considered that the formation of water droplets on surfaces is a random but repetitive process, as well as the fact that experimental and theoretical observations show that the droplet corrosion front of a metal surface is located in its zone circumference. We thus aimed to establish how the corrosion process evolves on a steel plate when many drops are deposited and removed repeatedly. An experimental setup and working procedure were used to obtain data characterizing the simultaneous process of steel surface corrosion and water droplet evaporation. For natural convection conditions with a variable relative humidity and temperature environment, an extensive data set consisting of the dynamics of individual droplet evaporation coupled simultaneously with the corrosion of the steel surface under the droplet was obtained. The mathematical models for evaporation and corrosion under the droplet have the same dynamic transfer surface for water evaporation and oxygen supply in the droplet. An approach for determining this surface depending on the momentary droplet mass was considered. Several simultaneous measurements of evaporation–corrosion dynamics were used to calibrate the coupled models, which were then used to show their compatibility with experimental data.

**Keywords:** water droplet corrosion; oxygen transfer; corrosion kinetics; mathematical modeling; steel corrosion; process dynamics



**Citation:** Ilie, M.C.; Chiș, T.V.; Maior, I.; Răducanu, C.E.; Deleanu, I.M.; Dobre, T.; Pârvulescu, O.C. Experimental Investigation and Modeling: Considerations of Simultaneous Surface Steel Droplets' Evaporation and Corrosion. *Metals* **2023**, *13*, 1733. <https://doi.org/10.3390/met13101733>

Academic Editors: Anthony Hughes and Reza Parvizi

Received: 30 August 2023

Revised: 5 October 2023

Accepted: 11 October 2023

Published: 12 October 2023



**Copyright:** © 2023 by the authors. Licensee MDPI, Basel, Switzerland. This article is an open access article distributed under the terms and conditions of the Creative Commons Attribution (CC BY) license (<https://creativecommons.org/licenses/by/4.0/>).

## 1. Introduction

Metal losses, especially steel losses, caused by the corrosion of metal structures located in the atmospheric environment are impressive [1,2]. The latest estimation of World Corrosion Organization (WCO) considers that the direct cost of worldwide corrosion is about of EUR 1.3 and 1.4 trillion, which is equivalent to 3.8% of the global Gross Domestic Product (GDP) [3]. Public data on metal corrosion costs show that it is an average of 3.4% of the global GDP, distributed by economic sectors, of which the industrial sector is at a level of 2% (USD 1600 billion out of a GDP of USD 80,000 billion). It is known that the

surface chemical process due to oxygen brought from the air into the water that comes periodically as rain or as droplets on the metal surface structures cannot be interrupted. However, it can be controlled in such a way that the operation of metal structures in an atmospheric environment is as safe as possible. The atmospheric corrosion of steels is a complex process with evolution at the molecular scale which is influenced by an extremely large number of factors, starting with the steel structure, the geographical positioning of the steel structure, the design and installation of the metal structure, the frequency and flow rate of the rains, the frequency and intensity of the deposition of drops on the surface, the presence of ionizable pollutants in the water, the non/existence of an anti-corrosion protection solution, etc. In the approach to atmospheric corrosion of weathering steels, there is a quasi-recognized consideration regarding the expression of the thickness of the corroded steel [4,5]. It starts from the acceptance of the simplest model of corrosion, according to which water forms a diffusion film to move towards the surface of the steel where it reaches and causes the maintenance of anodic and cathodic processes as a surface reaction [6]. The result of this model can be seen in Equation (1) which shows the time dependence, expressed in years, of the thickness of the corroded steel ( $\delta_{st}$ ), which, as a convention, is given in  $\mu\text{m}$ . The experimentally determinable constants  $A$  and  $n$  take into account the influence of the factors mentioned above on the dynamics  $A$  as well as the superficial formation of the rust layer, which reduces the intensity of corrosion  $n$ .

$$\delta_{st} = A \tau^n \quad (1)$$

Improvements have been made to Equation (1) to take into account excess moisture in the environment, the presence of sulfur dioxide (acid rain) or the presence of  $\text{Cl}^-$  ions in the corrosion environment [7]. We show that most countries in the world have participated, since 1980, in a program to monitor the atmospheric corrosion of steels, so that data on the parameters of this model are available [8]. Now, the problem of atmospheric corrosion of steels is treated much more complexly, starting mainly from the fact that water reaches the steel structures through rain and through condensation in drops (dew), which determines two main cases of corrosion, namely film corrosion and corrosion drops. Both cases of atmospheric corrosion can be characterized by approaches which consider them to be cases of simultaneous transfer of momentum and mass [9,10], respectively, and of simultaneous transfer of heat and mass [11,12] which are associated with the electrochemical process that takes place at the corrosion surface. In the case of droplet corrosion, their appearance on the condensation surface is a relatively fast process, under 10–15 min [13], if the condensation conditions are met [14], as is shown by Equation (2), where  $p_s$  is the water saturation pressure,  $t_s$  and  $t_g$  represent the surface and air temperature, respectively,  $U_r$  gives the air relative humidity and  $t_{dew}$  is the dew point temperature.

$$p_s(t_s) \leq p_s(t_g) U_r \text{ or } t_s \leq t_{dew}(U_r) \quad (2)$$

Being a condensation process, its speed is controlled by the heat transfer coefficient, which for condensation has extremely high values (5000–7000  $\text{w}/\text{m}^2 \cdot \text{grd}$ ). A coalescence of the small droplets on the steel surface, which is also fast, leads to a droplet size distribution estimated to follow a normal distribution, between 0.2 mm and 6 mm. Evaporation of a droplet from a surface is a simultaneous mass and heat transfer process with its duration depending on droplet size, on temperature difference  $t_s - t_g$  and on the fact that, here, the heat transfer coefficient is low (below 100  $\text{w}/\text{m}^2 \cdot \text{grd}$ ), corresponding to weak natural convection or laminar gas flow along the evaporation surface. In other words, considering its duration in relation to the surface corrosion process, droplet evaporation is much more important than deposition.

Considering these remarks, we focused in this study on the analysis of the kinetics within the corrosion process of the droplets, upon their evaporation. Many of the current approaches to modeling droplet corrosion refer to the Evans droplet model [12,15,16], which, in its current form [15], characterizes the onset of hemispherical droplet corrosion

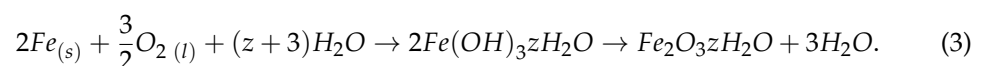
using unsteady-state species concentration field equations with reactions occurring on the surface at the cathodic and anodic (droplet-based) sites. For small hemispherical drops, the absence of movement in the droplet can be accepted [17], while for large drops this fact is no longer acceptable because here the evaporation of the droplet is accompanied by the Marangoni effect [18–20]. For small droplet corrosion, the COMSOL solution of the Evans model [17], where it uses only an anodic site on the surface and a cathodic site near the droplet hemisphere, shows both that the current density curves inside the droplet are arcs, starting from the anode and closing at the cathodic site, and that here, in the cathodic site (the area where the drop closes to the surface), the concentration of dissolved species reaches maximum values. With the same limit conditions, the mentioned model shows about the same result, and, in the case of large drops, the reports are limited to a duration of 600 s. Additionally, in this case, it is shown that the rust is deposited in the marginal area of the drop, while the photographs of the situation after the evaporation of the drop show the imprint of the rust all over its original location [16]. It should be noted that the model in question accepts the hemispherical shape of the droplet [16,17] which implies a wetting angle of the water surface of 90 degrees.

Depending on the metal surface, this angle is between 73 and 84 degrees [21,22], with about 80 degrees for water–steel. For large droplets with a hemispheric diameter in the range of 0.5–5 mm, formed by dew deposition and coalescence on the surface of steel or other metal, which corrode with simultaneous evaporation, there are many problems that are still the focus of research. Thus, it is not clear whether the Marangoni flow inside the droplet causes it to flatten into a cylinder or whether during evaporation the base of the droplet remains unchanged, grows or shrinks. In addition, there are few data on the average corrosion rate during droplet evaporation and how it is influenced by the presence of corrosion accelerators ( $Cl^-$  for example). Given the repeatability of surface dew deposition, it must be shown whether repeated formation of the droplet on a rust trace accelerates or decelerates corrosion. The current paper focuses on these issues or, more correctly, on some aspects of these issues. Specifically, a new approach was used to experimentally investigate the simultaneous process of droplet evaporation and sub-droplet corrosion on the steel surface, the purpose of which was to validate the models developed to describe this phenomenon. The droplet evaporation model and the sub-droplet corrosion model are coupled by having the same transfer surface, which decreases with time. A new solution was thus proposed to express the dynamics of the transfer surface for evaporation, and for oxygen supply in the droplet as a function of the momentary droplet mass, respectively, while several new elements were considered for the two coupled models, the most significant being the decreasing circulation due to the Marangoni phenomenon.

## 2. Materials and Methods

### 2.1. Experimental Setup and Procedures

The corrosion processes from one drop, complemented with total  $Fe^{+2}$  to  $Fe^{+3}$  oxidation and with metal oxide precipitation, is expressed [8–10] by Equation (3):



If we consider a sufficiently large number of drops deposited on a steel surface, then, at the end of their evaporation, the mass of the plate will increase. This increase in mass allows the determination of the corrosion rate (Equation (4)) and, by relating to the droplet surface, the specific corrosion flow rate (Equation (5)). Here  $\Delta m$  is the increase in plate mass,  $\tau$  corresponds to the droplet evaporation time,  $A_p$  represents the average droplet corrosion surface and using  $M_i$  ( $I = Fe, Fe_2O_3 \cdot zH_2O$ ) gives the molecular mass of species  $i$ .

$$G_m = \frac{\Delta m}{\tau} \frac{2M_{Fe}}{M_{Fe_2O_3 \cdot zH_2O}} \quad (4)$$

$$N_{Fe} = \frac{G_m}{nA_p} \quad (5)$$

Tracking the dynamics of droplet evaporation brings information about the kinetics of this process related to the external environmental conditions, mainly its temperature and relative humidity.

Repeating this process several times can show the extent to which the rust deposited on the surface is influencing the process. Replacing the water droplets with *NaCl*-containing droplets will show how the corrosion process is accelerated. The experimental setup is shown in Figure 1, and we mention the precision balance (Kern, Germany) coupling via USB, Kern Software SCD—4.2.4 Pro (Kern, Germany) Temperature and Humidity Data Logger (USB connection). The weathering steel plate was 2 mm thick, 200 mm wide and 300 mm long. The composition of the steel is given in Table 1. The water used as the corrosion medium had an electrical conductivity of 100 mS/cm and a pH of ~6.7, which makes it close to clean rainwater. In the accelerated corrosion tests, the *NaCl* content in the water was 1 g/L.

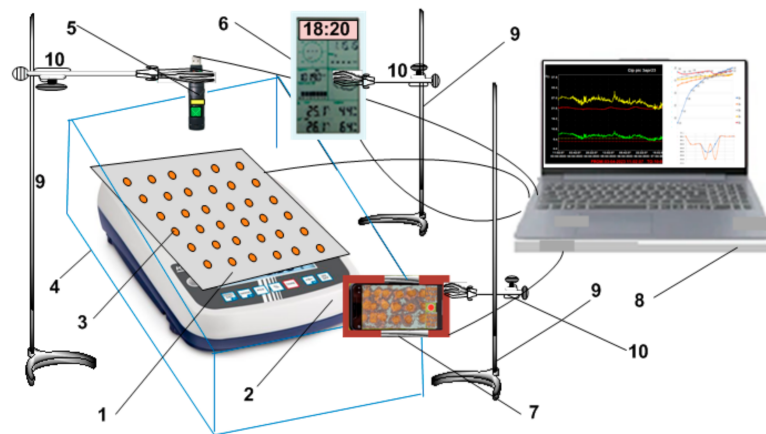


**Figure 1.** Experimental laboratory setup for corrosion in water droplets: (1) black steel plate for corrosion tests; (2) precision balance; (3) water droplets to corrode; (4) balance protection enclosure; (5) temperature humidity dew point Data Logger; (6) laboratory meteorological micro station; (7) filming device; (8) data registration and processing system; (9) stand; (10) clamp stand.

**Table 1.** Black weathering steel sheet composition used in water droplet corrosion research (according to manufacturer) [10].

Element	Composition (wt%)
Manganese (Mn)	0.166
Phosphorus (P)	0.028
Sulfur (S)	0.028
Carbon (C)	0.206
Chromium (Cr)	0.078
Molybdenum (Mo)	0.114
Vanadium (V)	0.003
Silicon (Si)	0.004
Copper (Cu)	0.082
Nickel (Ni)	0.088
Titanium (Ti)	0.004
Iron (Fe)	0.199

The atmospheric experiment parameters had values located in different ranges since the cumulative duration of the experiments was more than 9700 min: 18–29 °C for temperature, 27–60% for relative humidity and 6–17 °C for dew point.

The working sequences for a corrosion test include:

1. Determining the mass of the steel plate;
2. Loading the plate with droplets in the preset positions;
3. Starting the recording the momentary mass of the plate with droplets and the state of the moist air parameters near the surface (at ~8 cm from it);
4. Taking digital photographs of the plate with droplets at test starting, during the test and at the end of each test experiment;
5. Ascertaining the drying of the droplets and saving the recordings in order to process them.

Table 2 contains further data for a complete description of the experimental corrosion tests.

**Table 2.** Experimental data characterizing laboratory droplet corrosion tests.

C.N.	Experimental Factors	Values	Observations
1	Number of drops on the plate	100	Selected
2	The initial mass of the drops on the plate (g)	4.5–15.5	Selected
3	Average droplet volume ( $\mu\text{L}$ )	45–55	Computed
4	The initial shape of the drop	Spherical cap	Observed
5	Electrical conductivity and water pH ( $\mu\text{S}/\text{cm}$ )	100	Selected
6	Number of successive tests for corrosion in water	26	Selected
7	NaCl concentration (g/L) in water (accelerated corrosion)	1	Selected
8	Number of accelerated corrosion tests	4	Selected

If we refer to a droplet corrosion test, we have, experimentally, the dynamics of water evaporation from a droplet, the dynamics of the moisture content near the droplet, photo images that show the shape of the droplet during evaporation as well as the pressure, temperature and moisture content from the air from the evaporation medium. At the end of the test, the mass of rust associated with the mass plate, and therefore associated with each droplet, is available. The entire plan of the experimental investigation considered that its development takes place under natural convection conditions. Thus, each of the 30 tests reported in the paper were performed under conditions in the presence of moisture content and temperature different to the external air environment, recorded for each experiment. Then, each experiment started from the existence of a previous layer of rust on the surface. The duration between two experiments was, as shown in the results tables, random, but always allowed the newly deposited rust layer to reach the structural state of the previous one. The effective time of an experiment, strongly dependent on air humidity and temperature, was slightly modified, as is shown in the results from the data tables in the results section, by the mass of the droplet placed in the fixed location.

## 2.2. Mathematical Modeling

Modelling of mass and heat transfer phenomena is an effective tool in the design, control and optimization of chemical processes as well as in understanding their mechanisms [23,24]. As a descriptive model, droplet evaporation from a steel surface is a simultaneous mass and heat transfer problem. Here, the water vapor leaves the surface of the droplet in the adjacent environment (mass transfer) and the heat required for this process is brought from the environment (heat transfer). Under the experimental conditions of our test, the mass and heat transport mechanisms correspond to natural convection. The peculiarity of this problem comes from the fact that the drop changes its shape and volume. This fact additionally acts on the corrosion process by changing the specific flow of oxygen transferred to the corrosion surface, and by changing the surface under corrosion,

respectively, and, consequently, by reducing rust deposits. Figure 2 shows three possible models for the evolution of the droplet shape in the evaporation process.

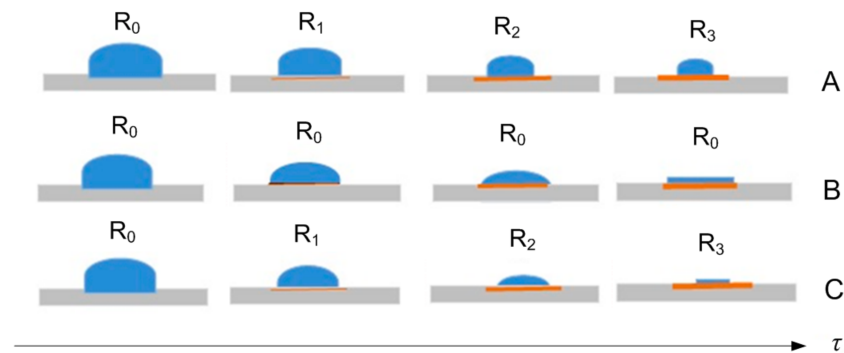


**Figure 2.** Possible models for the evolution of droplets shape during their evaporation, hemisphere shape: (A) descending hemisphere; (B) spherical cap with trace preservation; (C) spherical cap without trace preservation. Rust is brown color.

Regardless of the shape, if it is identifiable, as shown in Figure 3, then its analytical expression ( $y = f(x)$ ,  $x = \varphi(y)$ ) becomes possible from the knowledge of the instantaneous volume [22], as shown by Equation (6). The surface produced by rotating  $y = f(x)$  and  $x = \varphi(y)$  with respect to the  $x$  and  $y$  axes, respectively, [25] is the surface of the air drop interphase (Equation (7)).

$$V_{\tau 0x} = \pi \int_{-a_\tau}^{a_\tau} (f(x))^2 dx \quad V_{\tau 0y} = \pi \int_0^{h_\tau} (\varphi(y))^2 dy \tag{6}$$

$$S_{\tau 0x} = 2\pi \int_{-a_\tau}^{a_\tau} f(x) \sqrt{1 + f^I(x)} \quad S_{\tau 0y} = 2\pi \int_0^{h_\tau} \varphi(y) \sqrt{1 + \varphi^I(y)} dy \tag{7}$$

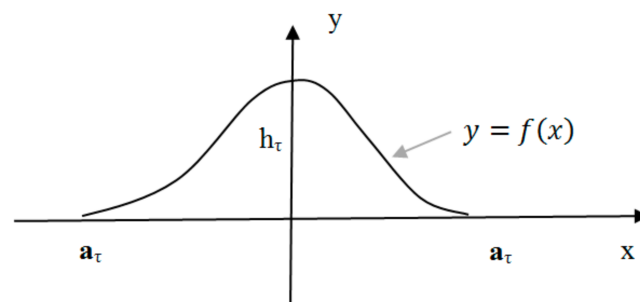


**Figure 3.** Droplet shape in  $y$ - $x$  graphic representation.

Our observations, justified with the presentation of the results, support that, for the evaporation of droplets on a steel surface, the initial shape and its evolution correspond to a paraboloid (Equation (8)). Here  $R$  is the initial radius of the droplet deposited on the surface and  $h_\tau$  shows the distance from the center of the droplet to its boundary.

$$\frac{x^2}{R^2} + \frac{y^2}{h^2} - 1 = 0 \tag{8}$$

The assumption that the droplet evaporates keeping its original trail allowed the analysis by modeling the two processes in the droplet. Thus, Figure 4 shows the simultaneous phenomenology of mass and heat transfer during droplet evaporation. Figure 5 shows the transfer of  $O_2$  inside the droplet, and its consumption through the reaction on the surface, resulting in the generation of rust. We mention that inside the droplet there is an internal flow determined by the association of the Marangoni phenomenon with its

evaporation [25–27]. Figure 5 schematically represents this flow. When falling outside, over the boundary layer, the experimental conditions characterize an environment, at most, in natural convection. Under these conditions, the vapors leaving the surface of the drop pass by diffusion over the inert (air) through the boundary layer of thickness  $\delta$ . On any direction,  $z$ , normal to the surface of the drop, the specific flow rate is given by the differential expression in Equation (9), where  $c$  is the total molar concentration and  $D_v$  represents the air vapor diffusion coefficient.

$$N_v = -\frac{cD_v}{(1 - y_v)} \frac{dy_v}{dz} \tag{9}$$

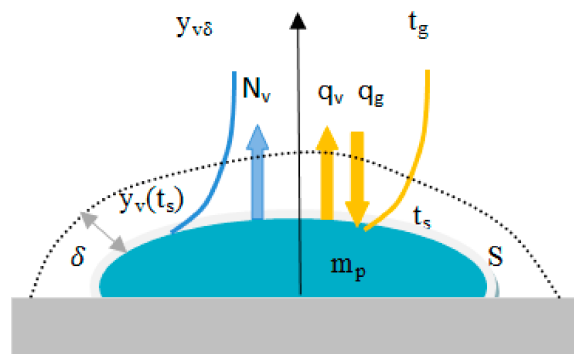


**Figure 4.** Representation of mass and heat transfer when evaporating the droplet from the steel surface (boundary layer limit as dotted line).

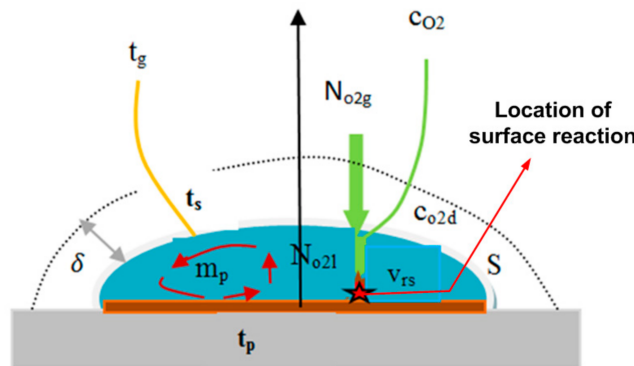


**Figure 5.** The process of oxygen transfer and corrosion inside the droplet with Marangoni flow (boundary layer limit as dotted line).

Figure 4 shows the vapor mole fraction at the droplet surface and outside the boundary layer, so that the integration of Equation (9) gives the integral expression of the vapor flow (Equation (10)).

$$N_v = \frac{cD_v}{\delta y_{Bm}} (y_v(t_s) - y_{v\delta}) \tag{10}$$

Relation (11) is written to highlight the driving force and the mass transfer coefficient in the form (12). Since  $c$ ,  $D_v$ ,  $\delta$  and even  $y_{Bm}$  in (10) depend on  $t_g$  and  $t_s$ , or more correctly on those differences, it was considered, for  $k_g$ , as dependent on the heat transfer driving force  $t_g - t_s$ . So,

$$k_g = \frac{D_v}{\delta y_{Bm}} = k_g(t_g - t_s) \tag{11}$$

$$N_v = ck_g(t_g - t_s)(y_v(t_s) - y_{v\delta}). \tag{12}$$

A balance for the duration from  $\tau$  to  $\tau + d\tau$ , when denoting the interphase transfer surface (evaporation surface)  $S(\tau)$ , yields Equation (12). Here  $S(\tau)$  depends on the instantaneous mass of the droplet ( $m_p$ ) as follows from the coupling of Equations (6)–(8), where we put  $V_{\tau 0y} = m_{p\tau} / \rho_a$ . With this consideration, Equation (13) can be written as Equation (14).

$$\frac{dm_p}{d\tau} = N_v M_w S(\tau) \tag{13}$$

$$\frac{dm_p}{d\tau} = \alpha f(m_p) N_v M_w \tag{14}$$

If we had expressions or values for the mass transfer coefficient for the interface temperature as well as for the function  $f(m_p)$ , then the momentary mass of the droplet becomes analytically expressible. Table 3 shows the calculation of the transfer surface, for the droplet masses of interest in the present work, so that  $\alpha$  and  $f(m)$  from Equation (14) can be identified. In more detail from Equation (8) it is expressed as  $x = \varphi(y)$  and since  $R$  is fixed and  $m_p$  is chosen, in the range of interest of our droplet mass, then solving the equation  $m_p = \rho_w V_{\tau 0y} = \pi \rho_v \int_0^{h_\tau} (\varphi(y))^2 dy$  (Equation (6)) gives the  $h_\tau$ , value, which then immediately leads to  $S$  or  $S(\tau)$ , as is shown in Equation (7), where it is correlated by regression polynomial after the momentary particle.

**Table 3.** Calculation of droplet evaporation surface value as a function of droplet mass for the case of paraboloid cap with constant cap radius.

Parameters		Surface Values as Function of Droplet Mass					
R (cm)		0.30					
$m_p$ (g)	0.060	0.050	0.040	0.030	0.020	0.010	0.005
$h$ or $h_\tau$ (cm)	0.312	0.276	0.235	0.183	0.133	0.069	0.035
S or $S(\tau)$ (cm <sup>2</sup> )	0.588	0.528	0.453	0.378	0.286	0.283	0.283
$\alpha f(m_p)$		$\alpha = \pi R^2 \quad f(m_p) = 0.908 + 7.08m_p + 221.2 m_p^2$					
R (cm)		0.35					
$m_p$ (g)	0.060	0.050	0.040	0.030	0.020	0.010	0.005
$h$ or $h_\tau$ (cm)	0.252	0.228	0.189	0.147	0.101	0.052	0.022
S or $S(\tau)$ (cm <sup>2</sup> )	0.595	0.530	0.458	0.385	0.385	0.385	0.385
$\alpha f(m_p)$		$\alpha = \pi R^2 \quad f(m_p) = 1.037 - 7.79m_p + 277.5 m_p^2$					
R (cm)		0.40					
$m_p$ (g)	0.060	0.050	0.040	0.030	0.020	0.010	0.005
$h$ or $h_\tau$ (cm)	0.217	0.185	0.152	0.116	0.078	0.040	0.020
S or $S(\tau)$ (cm <sup>2</sup> )	0.601	0.529	0.505	0.503	0.503	0.503	0.503
$\alpha f(m_p)$		$\alpha = \pi R^2 \quad f(m_p) = 1.043 - 5.98m_p + 135.7 m_p^2$					
R (cm)		0.45					
$m_p$ (g)	0.060	0.050	0.040	0.030	0.020	0.010	0.005
$h$ or $h_\tau$ (cm)	0.179	0.157	0.123	0.093	0.062	0.031	0.016
S or $S(\tau)$ (cm <sup>2</sup> )	0.666	0.656	0.642	0.636	0.636	0.636	0.636
$\alpha f(m_p)$		$\alpha = \pi R^2 \quad f(m_p) = 1.005 - 0.933m_p + 27.5 m_p^2$					

To be functional, the model, in terms of the mass dynamics of the evaporating water droplet at the surface, needs a solution to calculate the surface temperature of the water droplet and also to account for the mass transfer coefficient from the droplet to the surrounding air. In this sense, if the heating of the droplet is neglected, then the temperature  $t_s$  results from the fact that the specific heat flow brought by convection to the droplet (Equation (15)) is equal to the specific heat flow due to vaporization (Equation (16)). It is identified in Equation (15) that the value of the heat transfer coefficient is a function of the air temperature difference and the surface drop. So  $\alpha_g = \alpha_g(t_g - t_s)$ . In Equation (16) the latent heat of vaporization of water was denoted by  $r_v$ .

$$q_g = \alpha_g(t_g - t_s) = \alpha_g(t_g - t_s)(t_g - t_s) \quad (15)$$

$$q_v = N_v M_w r_v \quad (16)$$

The mentioned equality of  $q_g$  and  $q_v$ , coupled with  $N_v$  relationship, occurs for  $t_s$  in Equation (17).

$$\alpha_g(t_g - t_s)(t_g - t_s) = ck_g(t_g - t_s)(y_v(t_s) - y_{v\delta})M_w r_v \quad (17)$$

The transfer of mass and heat, respectively, from and to the droplet occurs through the boundary layer of the droplet, as shown in Figure 4. Thus, the analogy of transfer phenomena [28,29] can be used to express  $k_g(t_g - t_s)$  using  $\alpha_g(t_g - t_s)$ . This is given by Equation (18), where  $\rho_g$  is the air density and  $c_{pg}$  represents its specific heat coefficient. Coupling Equation (18) with Equation (19) leads to the expression of the droplet surface temperature by the conditional Equation (19). For  $y_v(t_s)$  Equation (20) is used, where  $p$  is the air pressure and  $A, B, C$  are the Antoine constants for expressing the water saturation vapor pressure.

$$k_g(t_g - t_s) = \frac{\alpha_g(t_g - t_s)}{\rho_g c_{pg}} \quad (18)$$

$$t_s = t_g - \frac{c}{\rho_g c_{pg}}(y_v(t_s) - y_{v\delta})M_w r_v, \quad y_v(t_s) > y_{v\delta} \quad (19)$$

$$y_v(t_s) = \frac{10^{A - \frac{B}{t_s + C}}}{p} \quad (20)$$

Regarding Equation (19), it should be specified that  $y_{v\delta}$  depends on the relative air humidity ( $\varphi$ ) and the saturation pressure of water vapor at its temperature  $t_g$ . It should also be said that, after  $t_s$ , this relationship is a transcendent equation so to analytically or graphically raise the dependence  $t_s = t_s(\varphi, t_g)$ , a calculation program is required.

To complete the model of droplet evaporation by natural convection, i.e., the model showing how the droplet mass evolves over time as a function of initial radius, shape, air relative humidity and air temperature, a relation expressing values of the heat transfer coefficient for this heat transfer mechanism is needed. A relation from the literature [30,31] was thus chosen, here specified in the form of Equation (21), where the coefficients  $a, m$  and  $l_c$  have the specifications shown in Table 4.

$$\alpha_g = \alpha_g(t_g - t_s) = a \left( \frac{t_g - t_s}{l_c} \right)^m \quad (21)$$

**Table 4.** Values for the parameters of Equation (21).

C.N.	Parameter	Vertical Surface	Horizontal Upper Surface	Horizontal Lower Surface
1	$a$	1.420	1.320	1.520
2	$m$	0.250	0.250	0.330
3	$l_c$	0.112	0.055	0.055

For the modeling of the corrosion process at the droplet–steel interface, it is considered to progress more slowly than the evaporation process. Thus, it may be close to steady state evolution. Therefore, it can be considered to be quasi-stationary. According to Figure 2, the transfer of oxygen through the droplet, from the concentration of  $c_{O2d}$  to the concentration of  $c_{O2s}$ , corresponding to the surface reaction, is considered the most important. Relation (22) expresses the specific flow rate of oxygen. This becomes (23) by expressing  $c_{O2s}$  from the equality of oxygen transferred with oxygen consumed by the reaction surface.

$$N_{O2l} = N_{O2} = k_l(c_{O2d} - c_{O2s}) \quad (22)$$

$$N_{O2l} = \frac{k_l k_{rsa}}{k_l + k_{rsa}} c_{O2d} \quad (23)$$

In Equation (23),  $c_{O2d}$  can be considered as the equilibrium of concentration of oxygen and the droplet surface temperature. The mass transfer coefficient  $k_l$ , given by adapting the literature [32,33], takes into account the fact that the driving force for the Marangoni flow inside the droplet is represented by the surface tension difference between the water at the droplet surface,  $\sigma(t_s)$ , and at the solid surface, ( $\sigma(t_p) \approx \sigma(t_g)$ ), as shown by Equation (24). For the apparent reaction constant,  $k_{rsa}$ , Equation (25) [10] was considered. Here the value of  $2.3 \times 10^{-5}$  m/s [10] was assumed for  $k_{rs}$  (oxygen surface reaction constant when the steel surface is not rusted (i.e., new, this is a novelty regarding the model from [10] previously)). In regard to the surface reaction rate constant, we show that it has a rather complex meaning. Thus, seeing the corrosion process as a process with a chemical kinetic in which the solid reacts with the limiting reactant (oxygen in water in the case of pure corrosion) and then it is influenced by local surface structure issues (local crystallinity, intra-granular inclusions). As these structural irregularities are distributed, the surface is seen to have average properties. As a result, the reaction rate constant of the surface corrosion process refers to a surface seen with average unevenness. The rust thickness,  $\delta_r$ , is linearly dependent on the mass of rust deposited at the solid interface of the droplet (Equation (26)). For the oxygen diffusion coefficient through the rust layer, the range of values is  $0.2 \times 10^{-9}$ – $2 \times 10^{-9}$  m<sup>2</sup>/s [10].

$$k_l = a \frac{\sigma(t_g) - \sigma(t_s)}{\eta} = 3.75 \times 10^{-5} \frac{\sigma(t_g) - \sigma(t_s)}{\eta} \quad (24)$$

$$\frac{1}{k_{rsa}} = \frac{1}{k_{rs}} + \frac{\delta_r}{D_{O2ef}} \quad (25)$$

$$\delta_r = \frac{m_{ru}}{\pi R_0^2 \rho_{ru}} \quad (26)$$

The momentary flow rate of consumed oxygen is given by Equation (27) where  $S(\tau)$  can be expressed as shown in Table 1. Based on Equation (3), the mass of iron dissolved under the droplet (Equation (28),) and the mass of deposited rust under the droplet are obtained, respectively, as is the contour of its trail (Equation (28)). As shown above, the rust mass was measured for each experimental test. Its dynamics, resulting from the

measurements performed, can be used to validate the developed models, as well as to promote a global kinetic relationship of droplet corrosion, as shown by Equation (1).

$$\frac{dm_{O_2}}{d\tau} = S(\tau)N_{O_2l}M_{O_2} = \alpha f(m_p)N_{O_2l}M_{O_2}, \quad \tau = 0 \quad m_{O_2} = 0 \quad (27)$$

$$m_{Fe} = \frac{4}{3}m_{O_2}\frac{M_{Fe}}{M_{O_2}} \quad (28)$$

$$m_{ru} = \frac{2}{3}m_{O_2}\frac{M_{ru}}{M_{O_2}} \quad (29)$$

It is worth noting that the droplet evaporation and surface corrosion models are coupled in that the values of variables and parameters from one model are found in the other. We thus have a unitary model of evaporation and corrosion in the droplet. Extending this model to other cases of external droplet flow involves the use of new characteristic relations for the heat and mass transfer coefficients for droplet evaporation.

### 3. Results

For droplets deposited on weathering steel plates we show that the experimental investigation followed droplet evaporation and steel corrosion by measuring:

1. The water mass dynamics of the drops from the plate;
2. The state of the evaporating drops' shape;
3. The air parameters near to the plate with the evaporating drops;
4. The increase in plate mass due to rust deposition from corrosion process.

Table 2 shows that in each test 100 drops were deposited on the steel plate. The aggregate droplets deposited on the plate at the beginning of each test were characterized, as shown in Figure 6, by mean diameter and standard deviation. It is also not difficult to appreciate from Figure 6 the paraboloid shape of these drops. The same procedures were used for droplet traces, which remain on the plate after evaporation. It was found, as can be seen in the data below, that the diameter of the trace is between 5 and 10% larger than that of the drop.

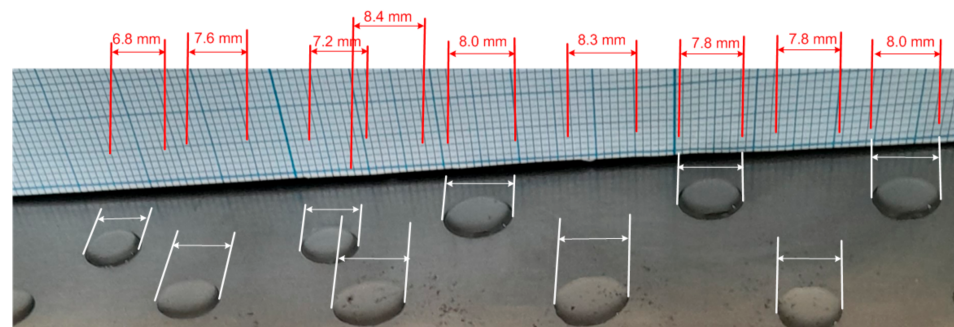


**Figure 6.** Determination of the average diameter of the water droplet and its associated standard deviation (Test 1,  $d_0 = 7.71 \pm 0.8$  mm).

Figures 7 and 8 show frames from a filmed experiment step of the corrosion evaporation tests. Figure 7 presents the steps from blank steel plate to the end of droplet evaporation, allowing us to observe the evolution from a water droplet to a shape on the steel plate in a considered first such test experiment. Frames shown in Figure 8 present the same evolution, but for a third considered experiment, which starts with a rusted shape on the steel plate already. Both Figures 7 and 8 come to support that, during evaporation, the droplet shrinks while keeping its diameter very close, practically the same, to the original diameter of the droplet. It is stated in Table 3, that in the building of functions  $f(m_p)$  this fact, now supported experimentally, was used: namely that the drop shrinks while keeping its initial diameter.



**Figure 7.** Frames from droplet evaporation–corrosion on a steel surface in Test 1, showing that droplet shrinkage occurs with droplet diameter maintained: ( $\varphi = 36.5\%$ ,  $d_0 = 7.2$  mm): (a) blank black steel plate, starting droplet’s deposition; (b) droplet already in position; (c) evaporation evolution after 21 min; (d) end of evaporation and shape formation; (d) bottom-third deposition of the drop,  $\varphi = 43.5\%$ ,  $d_0 = 7.2$  mm.

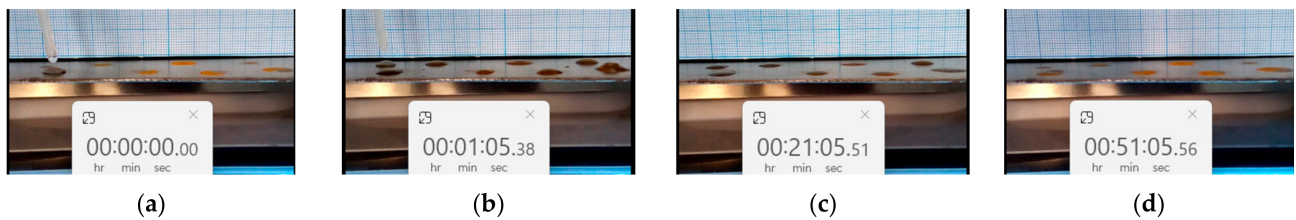


**Figure 8.** Frames from droplet evaporation–corrosion on a steel surface in Test 3, showing that droplet shrinkage occurs with droplet diameter maintained: ( $\varphi = 43.5\%$ ,  $d_0 = 7.2$  mm): (a) starting droplet’s deposition onto rusted old trails; (b) droplet already in position; (c) evaporation evolution after 21 min; (d) end of evaporation with the new layer of rust.

Considering the conclusion after analyzing Figures 7 and 8 we can refer to the differences between the initial diameter of the droplet, established in Figure 6, and the diameter of the droplet trail after the droplet has evaporated. So, this difference in mean diameter and standard deviation shows that there is an extension of preferential rust deposition at the edge of the drop contour, or that the deposition of a new drop into an old trace was not centered enough. Referring to the Evans corrosion model [12], we appreciate that there was a tendency for rust at the edge of the drop contour.

Tables 5–8 and Figures 9–12 present primary data for four evaporation–corrosion tests when the plate surface is made of steel, with its composition shown in Table 1. It is noted that the presence of NaCl in the corrosion medium (column F from Tables 7 and 8 compared to the same column from Tables 4 and 5) significantly changes the mass of rust obtained at the end of the test. If we return to the corrosion pattern, it shows, first of all, a significant change in the value of the surface reaction rate constant, which expresses Fe dissolution. Doubling or tripling of the corrosion rate in the presence of Cl<sup>−</sup> is reported in many works [34,35], so our data are in agreement with them.

**Table 5.** Experimental data characterizing the evaporation of droplets from the steel surface and its corrosion (Test 1,  $d_0 = 7.78 \pm 0.31$  mm,  $d_u = 8.05 \pm 0.45$  mm).

A	B	C	D	E	F	G	H	I	J	K	L	M
1	0		487.25	0.00		27.7	53.9	17.5				0.0
2	30		486.35	0.90		27.8	52.9	17.3				0.5
3	60		485.30	1.05		27.9	53.3	17.5				1.0
4	90		484.00	1.30		27.9	52.8	17.3				1.5
5	120	482.15	483.50	0.50	0.05	28.0	52.1	17.2	26.0	55.0	757.6	2.0
6	150		482.80	0.70		27.8	52.8	17.2				2.5
7	180		482.20	0.60		27.8	52.9	17.3				3.0
8	210		482.20	0.00		27.8	53.2	17.3				3.5

(A) current number; (B) time (min); (C) initial plate mass (g); (D) current plate mass (g); (E) evaporated water (g); (F) resulted rust mass (g); (G) air temperature (°C); (H) air humidity (%); (I) dew point temperature (°C); (J) external air temperature (°C); (K) external air humidity (%); (L) air environment pressure (mmHg); (M) cumulated time (h).

**Table 6.** Experimental data characterizing the evaporation of droplets from the steel surface, and its corrosion (Test 4,  $d_0 = 7.79 \pm 0.54$  mm,  $d_u = 8.38 \pm 0.55$  mm).

A	B	C	D	E	F	G	H	I	J	K	L	M
1	0		486.85	0.00		27.2	43.2	13.6				81.0
2	30		484.35	2.50		27.4	42.8	13.6				81.5
3	60	482.30	484.10	0.25	0.05	27.5	42.5	13.6	2.0	44.0	756	82.0
4	90		482.80	1.30		27.7	41.9	13.5				82.5
5	120		482.35	0.00		27.9	40.9	13.3				83.0
6	150		482.35	0.00		27.8	40.9	13.3				83.5

(A) current number; (B) time (min); (C) initial plate mass (g); (D) current plate mass (g); (E) evaporated water (g); (F) resulted rust mass (g); (G) air temperature (°C); (H) air humidity (%); (I) dew point temperature (°C); (J) external air temperature (°C); (K) external air humidity (%); (L) air environment pressure (mmHg); (M) cumulated time (h).

**Table 7.** Experimental data characterizing the evaporation of droplets from the steel surface and its corrosion (Test 28,  $d_0 = 8.70 \pm 0.44$  mm,  $d_u = 8.93 \pm 0.50$  mm).

A	B	C	D	E	F	G	H	I	J	K	L	M
1	0		501.60	0.00		28.5	32.2	10.3				9711.5
2	30		498.00	3.60		28.3	31.7	9.8				9712.0
3	60		497.30	0.70		28.2	33.4	10.5				9712.5
4	90		495.40	1.90		28.3	32.6	10.3				9713.0
5	120		492.35	3.05		28.1	32.2	9.9				9713.5
6	150	484.45	490.20	2.15	0.25	28.1	32.1	9.9	32	45	759	9714.0
7	180		488.40	1.80		28.0	31.7	9.6				9714.5
8	210		487.65	0.75		28.0	31.8	9.6				9715.0
9	240		486.30	1.35		27.9	32.4	9.8				9715.5
10	270		485.40	0.90		27.8	33.1	10.1				9716.0
11	300		484.85	0.55		27.7	33.6	10.2				9716.5
12	330		484.85	0.00		27.6	34.1	10.3				9717.0

(A) current number; (B) time (min); (C) initial plate mass (g); (D) current plate mass (g); (E) evaporated water (g); (F) resulted rust mass (g); (G) air temperature (°C); (H) air humidity (%); (I) dew point temperature (°C); (J) external air temperature (°C); (K) external air humidity (%); (L) air environment pressure (mmHg); (M) cumulated time (h).

**Table 8.** Experimental data characterizing the evaporation of droplets from the steel surface and its corrosion (Test 30,  $d_0 = 9.05 \pm 0.47$  mm,  $d_u = 9.32 \pm 0.49$  mm).

A	B	C	D	E	F	G	H	I	J	K	L	M
1	0		496.15	0.00		28.9	37.8	13				9769.0
2	30		493.10	3.05		29.1	37.6	13.1				9769.5
3	60		491.20	1.90		29.2	37.7	13.3				9770.0
4	90	485.20	489.35	1.85	0.30	29.0	36.9	12.7	30	35	757	9770.5
5	120		488.15	1.20		28.8	37.1	12.7				9771.0
6	150		486.70	1.45		28.7	37.1	12.6				9771.5
7	180		485.50	1.20		28.6	37.1	12.5				9772.0
8	210		485.50	0.00		28.5	36.7	12.2				9772.5

(A) current number; (B) time (min); (C) initial plate mass (g); (D) current plate mass (g); (E) evaporated water (g); (F) resulted rust mass (g); (G) air temperature (°C); (H) air humidity (%); (I) dew point temperature (°C); (J) external air temperature (°C); (K) external air humidity (%); (L) air environment pressure (mmHg); (M) cumulated time (h).

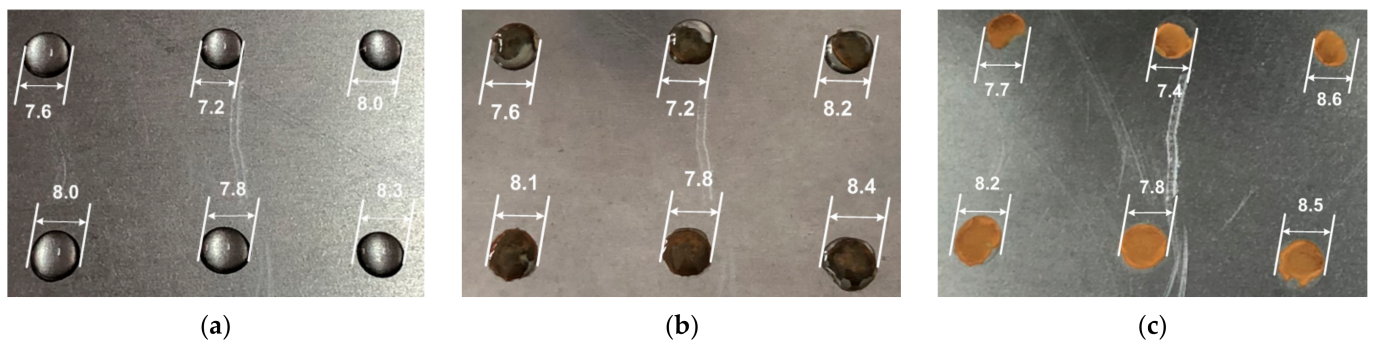


**Figure 9.** Droplet shape and diameter during their evaporation from the steel surface in evaporation-corrosion Test 1: (a) initial; (b) after 120 min; (c) after 210 min (end of test). Mean diameter and standard deviation are shown in Table 5.

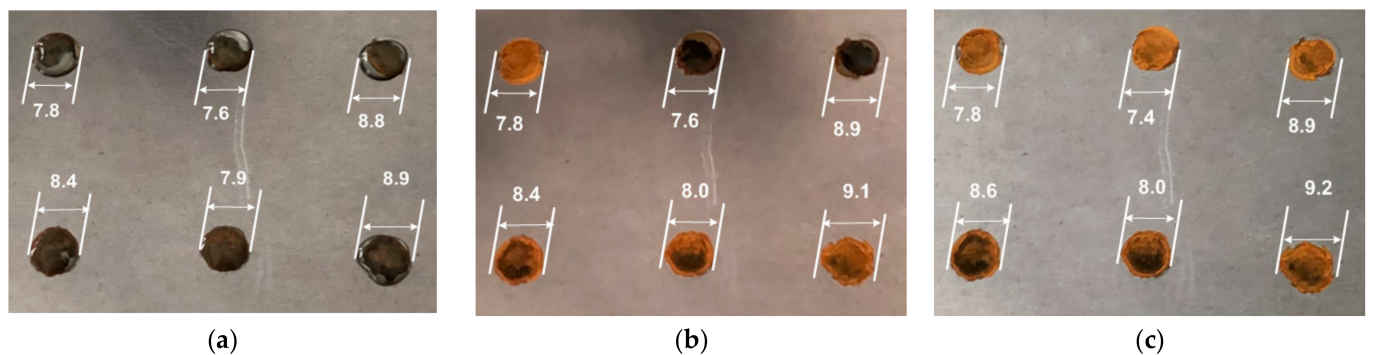


**Figure 10.** Droplet shape and diameter during their evaporation from the steel surface in evaporation-corrosion Test 4: (a) initial; (b) after 120 min; and (c) after 210 min (end of test). Mean diameter and standard deviation are shown in Table 6.

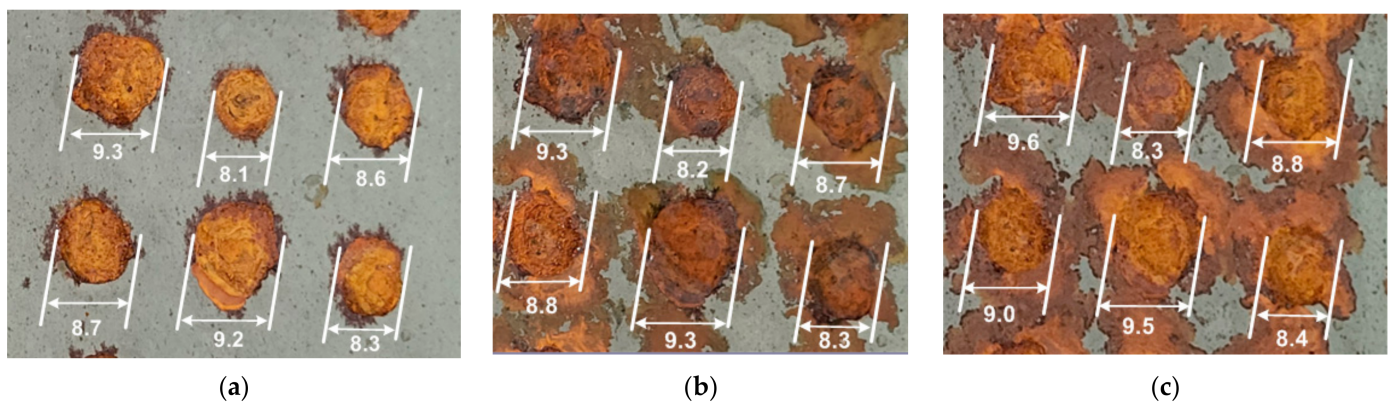


**Figure 11.** Droplet shape and diameter during their evaporation from the steel surface in the evaporation-corrosion test 28: (a) initial; (b) after 120 min; (c) after 330 min (end of test). Mean diameter and standard deviation are shown in Table 7).

From Tables 5–8, and the corresponding figures, supported by all 30 evaporation-corrosion tests in the work, it can be seen that the size of the initial drop, the relative humidity and the temperature of air near the steel surface and the rust loading of location for droplets deposition are important factors that determine the evaporation time and the corrosion rate when the droplets deposited on the surface are similar to rainwater. The chlorine and sodium ions' presence in drops, in this case at a concentration level of 1 g/L *NaCl*, does not change the dynamics of evaporation instead, as previously mentioned,

instead it causes the increasing of corrosion specific flow rate from 0.01–0.012  $\text{mg}_{\text{Fe}} \cdot \text{cm}^{-2} \cdot \text{h}^{-1}$  (Tables 5 and 6, column F) to 0.05–0.06  $\text{mg}_{\text{Fe}} \cdot \text{cm}^{-2} \cdot \text{h}^{-1}$  (Tables 7 and 8, column F).

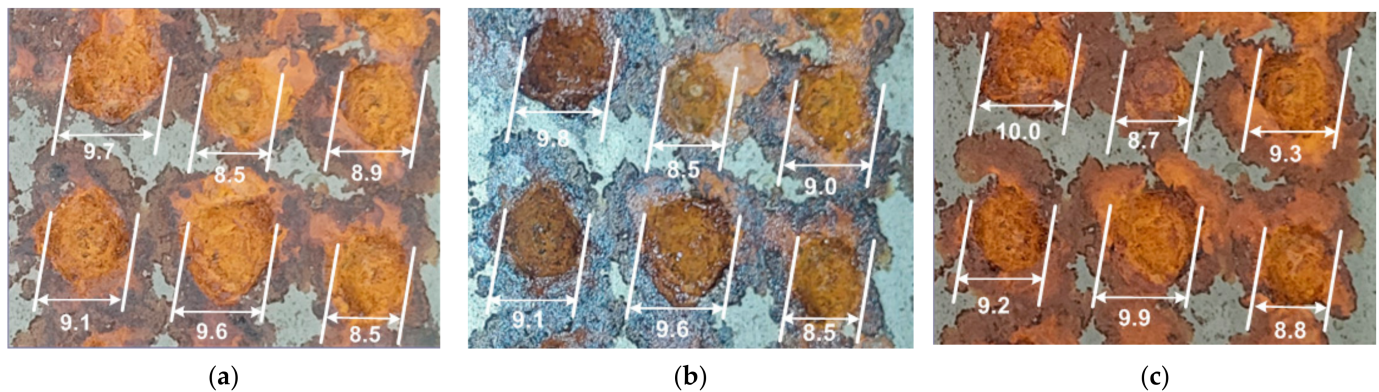


**Figure 12.** Droplet shape and diameter during their evaporation from the steel surface in the fourth evaporation-corrosion test 30: (a) initial; (b) after 120 min; (c) after 210 min (end of test). Mean diameter and standard deviation are shown in Table 8).

Overall, these tables and figures (each of them) contain all the necessary data, (evaporated water, and the deposited rust mass as dynamics relatable to a single drop, respectively) so that they can be used in testing our developed model.

#### 4. Discussion

In a comprehensive sense, model testing has a calibration part and a validation part. The calibration part involved several sequences, namely:

1. Completing the model with additional data (temperature dependence of dissolved oxygen concentration in water droplet, temperature dependence of water surface tension, densities, molecular masses, etc.) and conditions' initials;
2. The numerical transposition of the model with the micro sequences: (a) the choice of the parameters of the model that require calibration, namely the coefficient  $\alpha$  and the power  $m$  in relation (21), the coefficient  $a$  in Equation (24),  $k_{rs}$  and the relation  $D_{O_2efin}$  (Equation (25)), respectively; (b) selection, from the beginning of the investigation, of the tests with all their data, which are used in the calibration (Tables 5 and 6 for corrosion in water droplets, respectively, and Table 8 for corrosion with droplets containing  $\text{NaCl}$ ); (c) setting an option regarding air parameters' (relative humidity and temperature according to Tables 5–8) use in the model, i.e., as functions of time or as average values; (d) the effective expression of the numerical model from the import of the test data file to the Runge–Kutta integration of the differential equations that provides the dynamics of the mass of the droplet and the dynamics of the mass of rust deposited under the droplet, respectively;
3. The effective use of the numerical model in order to establish values for certain parameters, and strategies for expressing others, respectively.

Table 9 summarizes the model calibration results. Referring to what is presented here, including the reporting of these data by those in the specialized literature, there are some comments to make. The use of mean values for relative humidity ( $\varphi$ ) and air temperature ( $t_g$ ) near the plate is supported by the recorded data (Tables 5–8, column G and H), which show extremely small time variations. The values identified for the surface reaction rate constant ( $k_{rs}$ ) and for the effective diffusion coefficient of oxygen through the rust layer ( $D_{O_2ef}$ ) are consistent with those from film corrosion [9] when evaporation–corrosion occurs in water droplets. The higher values of  $k_{rsin}$  corrosion by  $\text{NaCl}$  water droplets show the intensification of the anodic reaction on the steel surface, as reported in other works [34–36]. The high value of  $D_{O_2efin}$  in this case indicates a fairly permeable structure of the rust formed in the corrosion process, as well as that here the transport of oxygen is facilitated

by the action of the  $Cl^-$  ions. For the constant  $\alpha$  in Equation (24) the model worked well with a higher value compared to those found in the literature ( $3.75 \times 10^{-5}$ ).

**Table 9.** Values of some model parameters and strategy from Equation (21).

C.N.	Case	Data	$\varphi$	$t_g$	$k_{rs}$ (Equation (25))	$D_{O_2f}$ (Equation (23))	$a$ (Equation (21))	$m$ (Equation (21))	$\alpha$ (Equation (24))
1	Water droplet	Table 5 Table 6	mean	mean	$4.5 \times 10^{-5}$ (m/s)	$9.1 \times 10^{-10}$ (m <sup>2</sup> /s)	$f(\varphi, t_g)$	0.33	$2.63 \times 10^{-4}$ (m <sup>2</sup> ·s)
2	Water droplet with NaCl	Table 8	mean	mean	$9.5 \times 10^{-4}$ (m/s)	$5.1 \times 10^{-9}$ (m <sup>2</sup> /s)	$f(\varphi, t_g)$	0.33	$2.63 \times 10^{-4}$ (m <sup>2</sup> ·s)

If to the presentation of Equation (21) it is added that, in addition to heat transport by natural convection, we have an additional heat transport via vapors leaving the surface, then the value chosen for the constant  $m$  is supported as well as the fact that  $a$  can be a function of  $\varphi$  and  $t_g$ .

With the calibrated model, all the corrosion tests performed were simulated with the constant  $a$ , from Equation (21), being modified to obtain the best model reproduction of the experimental dynamics showing the mass of the evaporating droplet. For the dynamics of rust deposited during droplet evaporation, we monitored whether, at the end of each test simulation, the rust mass was close to the recorded one (see Tables 5–8 column F scaled to 100 (number of drops)).

The result of these simulations is concentrated in Figures 13–17 and Table 10, which characterize, in comparison with those specified above, each individual test.

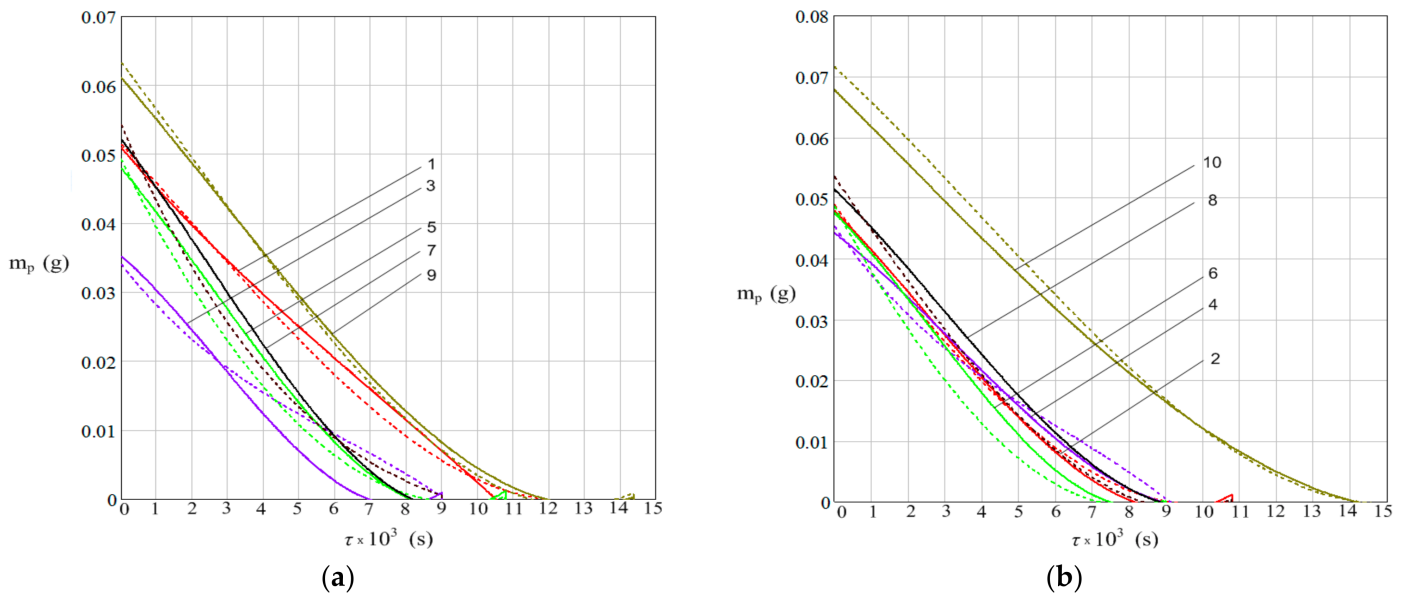


**Figure 13.** Dynamics of droplets mass during their evaporation for tests 1 to 10 ( $T_1 \dots T_{10}$ ): (a)  $T_1$ —red;  $T_3$ —blue;  $T_5$ —green;  $T_7$ —black;  $T_9$ —brown; (b)  $T_2$ —red;  $T_4$ —blue;  $T_6$ —green;  $T_8$ —black;  $T_{10}$ —brown; continuous curves—model, dashed curves—experimental.

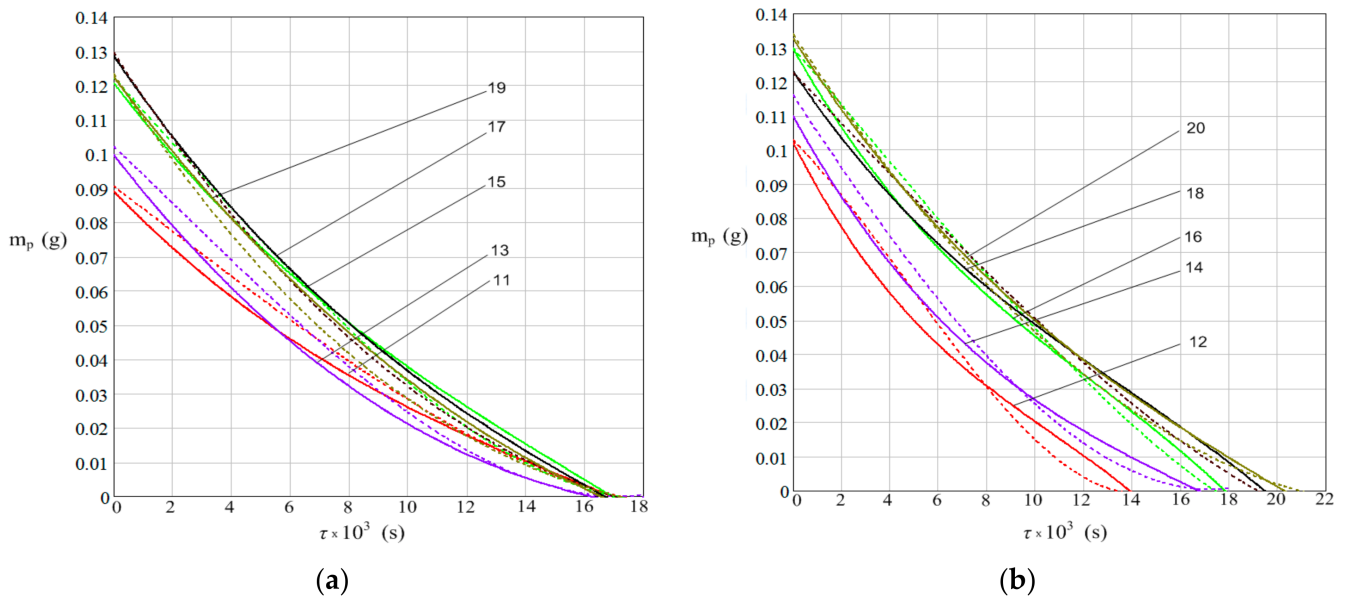


**Figure 14.** Dynamics of droplets mass during their evaporation for tests 11 to 20 ( $T_{11} \dots T_{20}$ ): (a)  $T_{11}$ —red;  $T_{13}$ —blue;  $T_{15}$ —green;  $T_{17}$ —black;  $T_{19}$ —brown; (b)  $T_{12}$ —red;  $T_{14}$ —blue;  $T_{16}$ —green;  $T_{18}$ —black;  $T_{20}$ —brown; continuous curves—model, dashed curves—experimental.

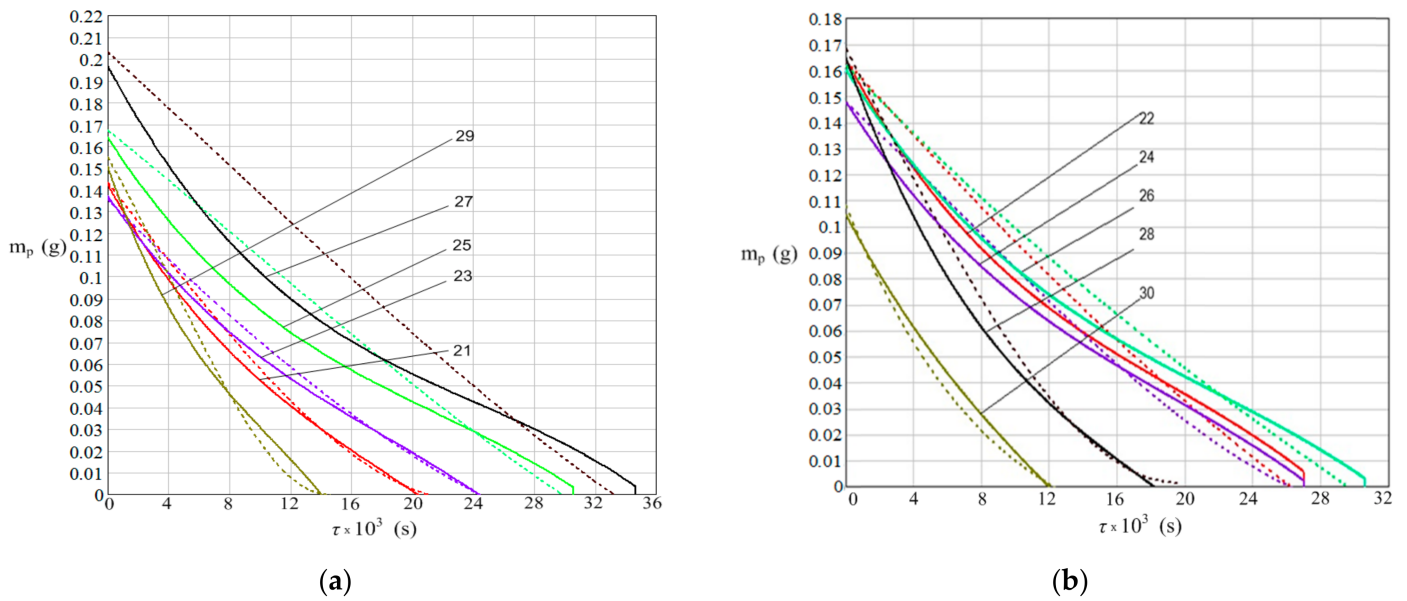


**Figure 15.** Dynamics of droplets mass during their evaporation for tests 21 to 30 ( $T_{21} \dots T_{30}$ ): (a)  $T_{21}$ —red;  $T_{23}$ —blue;  $T_{25}$ —green;  $T_{27}$ —black;  $T_{29}$ —brown; (b)  $T_{22}$ —red;  $T_{24}$ —blue;  $T_{26}$ —green;  $T_{28}$ —black;  $T_{30}$ —brown; Continuous curves—model, dashed curves—experimental.

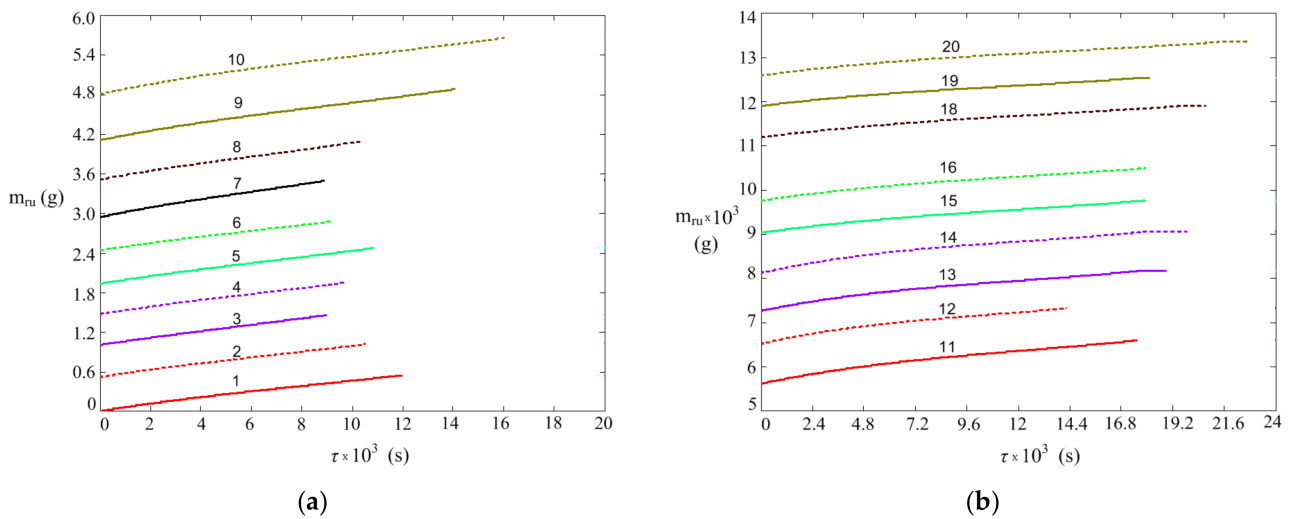


**Figure 16.** Dynamics of deposited rust mass during droplets evaporation-corrosion, from one droplet, experimental for tests  $T_1 \dots T_{20}$ : (a)  $T_1$  to  $T_{10}$ ; (b)  $T_{11}$  to  $T_{20}$ ; continuous curves—model, dashed curves—experimental.

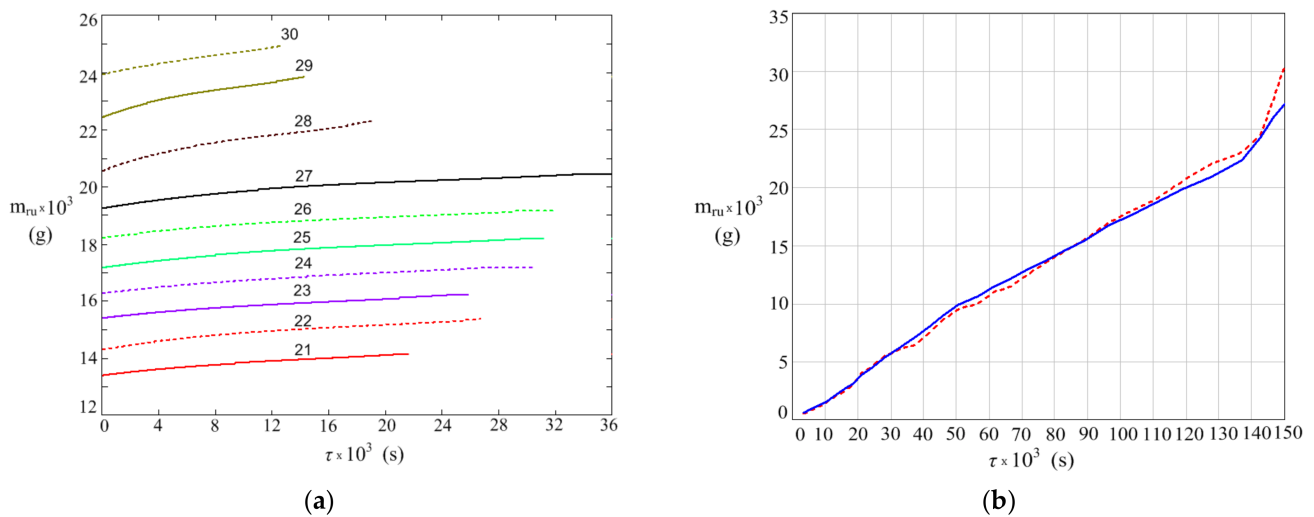


**Figure 17.** Dynamics of deposited rust mass during droplets evaporation—corrosion: (a) in experimental tests  $T_{21} \dots T_{30}$ ; (b) cumulated mass rust vs. effective corrosion time; line—model, dashed line—experimental).

**Table 10.** Corrosion tests and comparison of experimental results with those according to the model by relative deviations ( $\epsilon_{mpM}$ ,  $\epsilon_{mruM}$ ).

Test	$m_{p0}$ (g)	$\varphi$ (l)	$t_g$ (°C)	$a$ (20)	$\epsilon_{mpM}$ (%)	$\epsilon_{mruM}$ (%)	$\tau_t$ (h)	$\tau_c$ (h)	$\tau_p$ (h)
1	0.0500	0.531	27.8	7.66	−8.14	−9.31	3.5	3.5	3.5
2	0.0480	0.454	28.2	7.69	−7.65	−2.85	3.0	6.5	30.5
3	0.0360	0.354	28.3	5.18	11.31	2.94	2.5	9.0	57.5
4	0.0455	0.427	27.6	5.95	18.62	1.94	2.5	11.5	83.5
5	0.0490	0.328	27.7	5.23	15.18	4.39	3.0	14.5	134
6	0.0480	0.306	27.4	5.41	−11.50	15.55	2.5	17.0	161
7	0.0535	0.312	28.2	5.33	14.14	8.65	2.5	19.5	187
8	0.0535	0.350	28.9	5.19	0.717	11.02	3.0	22.5	214
9	0.0630	0.383	25.6	5.41	15.29	5.62	4.0	26.5	1658
10	0.0700	0.339	26.3	4.39	1.81	−161	4.5	31.0	1687

Table 10. Cont.

Test	$m_{p0}$ (g)	$\varphi$ (l)	$t_g$ (°C)	$a$ (20)	$\varepsilon_{mpM}$ (%)	$\varepsilon_{mruM}$ (%)	$\tau_t$ (h)	$\tau_c$ (h)	$\tau_p$ (h)
11	0.0915	0.479	21.4	6.80	8.45	2.35	5.0	36.0	2892
12	0.1040	0.441	21.5	7.16	−12.74	3.83	4.0	40.0	2920
13	0.1020	0.301	24.9	4.39	18.00	4.79	5.0	45.0	5517
14	0.1150	0.261	25.4	3.79	−0.96	2.45	5.0	50.0	5645
15	0.1230	0.950	25.8	4.65	−13.42	4.68	5.0	55.0	5575
16	0.1310	0.299	24.9	4.88	−1.39	2.92	5.0	60.0	6252
17	0.1320	0.349	23.9	6.26	−3.21	4.86	5.0	64.0	6282
18	0.1240	0.361	23.2	6.25	−3.49	7.19	5.5	69.5	6584
19	0.1260	0.306	21.3	6.97	−3.31	7.96	5.0	74.5	6603
20	0.1350	0.326	22.9	5.21	−4.41	8.72	6.0	80.5	6663
21	0.1460	0.312	23.1	5.01	0.48	9.66	5.5	86.0	6903
22	0.1670	0.498	20.9	5.31	1.75	9.92	7.5	93.5	7014
23	0.1390	0.498	20.2	6.99	3.04	9.71	7.0	100.5	7654
24	0.1500	0.489	20.0	6.30	−6.20	11.24	7.5	108.0	7684
25	0.1670	0.487	20.9	6.05	16.75	12.89	8.5	116.5	7719
26	0.1650	0.577	20.3	7.26	5.16	11.08	8.5	125.0	7789
27	0.2080	0.495	20.8	5.19	17.87	8.95	9.5	134.5	7820
28	0.1250	0.326	28.1	5.95	15.18	12.27	5.5	140.0	7860
29	0.1550	0.337	28.4	6.21	15.28	13.27	4.0	144.0	7884
30	0.1090	0.372	28.8	6.86	−19.98	17.31	3.5	147.5	7908

The relative deviation between the experimental values and those according to the model, presented in Table 10 for the dynamics of the droplet mass and for the dynamics of the deposited rust mass, respectively, was calculated according to the available data, as it appears in Equations (30) and (31), respectively. In Equation (30)  $n_i$  is the number of time steps since model integration for the  $i$  evaporation-corrosion test.

$$\varepsilon_{mpMi} = \frac{1}{n_i} \frac{\sum_{j=1}^{n_i} m_{pex}(\tau_j) - \sum_{j=1}^{n_i} m_{pt}(\tau_j)}{\sum_{j=1}^{n_i} m_{pex}(\tau_j)} 100 \quad i = 1, 2 \dots 30 \quad (30)$$

$$\varepsilon_{mruMi} = \frac{m_{ruexi} - m_{ruti}}{m_{ruexi}} 100 \quad i = 1, 2 \dots 30 \quad (31)$$

Before making a more detailed presentation of what Figures 13–17 and Table 10 show, we can state that we have here a good coverage of the experimental data from those produced by the developed and calibrated model. We want to highlight from the model calibration, and even motivated by it, that for  $a$  coefficient in Equation (21) a dependence on the relative humidity of the air and its temperature is expected. We find this dependence in Table 10, which shows that at high relative humidity and temperature, above 27 °C is high (tests 1, 2, 26, 30), and that, at low relative air humidity and temperature, around 24 °C  $a$  is the lowest values (tests 10, 13, 14, 21, 27). Calculation of correlation coefficients for  $a$  vs.  $\varphi$  and  $a$  vs.  $t_g/20$  finds the values 0.7551 and  $-0.2900$ , respectively, showing that  $a$  can, in the limit, be linearly related to  $\varphi$  and can be considered independent of  $t_g$ . Figure 18 supports these results. The line  $a$  vs.  $\varphi$  in this figure is given by Equation (32). Adding Equation (32) to Table 9 means that all parameters of the evaporation–corrosion model are known.

$$a = 2.423 + 8.839\varphi \quad (32)$$

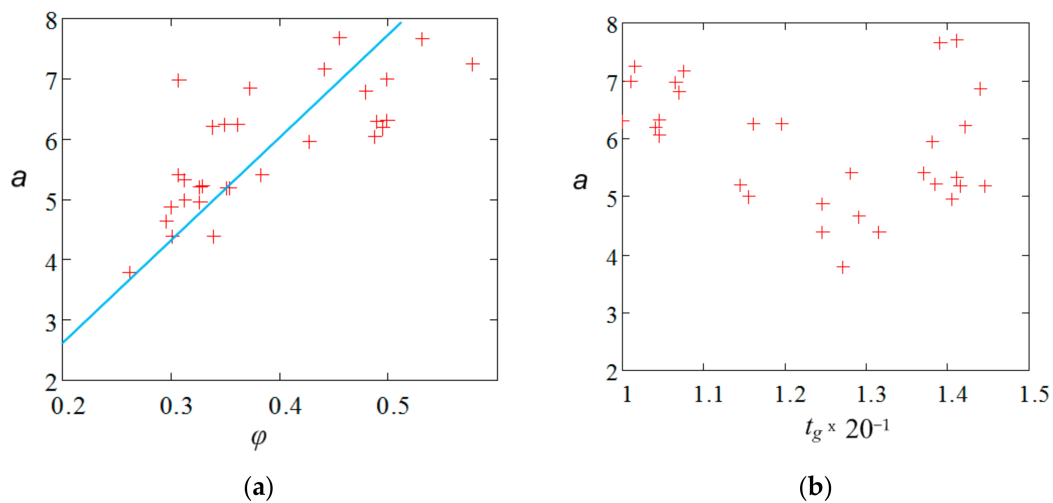


**Figure 18.** The evolution of  $a$  coefficient of Equation (21) in respect to the relative humidity of the air (a) and its temperature (b).

The dynamics of the evaporation of a single droplet, having variable mass under variable environmental conditions (Table 10), are described well, even very well, by the developed model, as shown by the values of the relative deviations experiment model (Table 10, column  $\varepsilon_{mpM}$ ) together with graphical representations from Figures 13–15.

Considering the model curve and the experimental curve for each evaporation test (Figures 13–15), we note their good correspondence, which supports the quality of the model. From 30 sets of curves, only in the case of test 27, and maybe test 25, does it appear that the model–experiment agreement is borderline. Figures 13–15, as well as Figures 16 and 17, in conjunction with the data in Table 10, show that the evaporation time of the drop depends on its size and the relative humidity and temperature of the air. The plots in Figures 17 and 18b, showing the dynamics of the rust mass from each of the 30 experiments, were drawn using the data provided by the model. The slope of these lines, which represent the corrosion rate, is almost the same for tests 1–27 where the water droplet contained no added ions. The nearly threefold increase in this slope when we have 1 g/L  $NaCl$  in the droplet (tests 28, 29 and 30) shows the intensification of the corrosion rate by suppressing the cathodic reactions in the corrosion pile. The representation in Figure 18, on the right side, shows the strong agreement between the dynamics of the rust mass deposited under the drop, obtained experimentally and by modeling. Thus, the approach of modeling the corrosion process through a droplet oxygen transfer model with chemical reaction on the steel surface is very well supported. Here too we can observe the above-mentioned change in the evolution of the slope when the composition of the droplet is changed by the addition of ions.

Looking at some possibilities for extending the evaporation–corrosion model, we mention several situations. Given that dewdrops deposited on a surface form in a distribution of sizes and dimensions, the model can simulate cases that are then averaged by the average probability of each size and dimension in the considered distribution. If there are no natural convection conditions during evaporation, then new expressions for the heat transfer coefficient must be added to the model (the case of Equation (21) in the current work). For low temperatures, obviously above the freezing point of water, the model can work, provided that the temperature dependence of the surface reaction rate constant is identified, which may be of the Arrhenius type.

## 5. Conclusions

Droplet corrosion on the steel surface was analyzed experimentally and by modeling.

A pilot laboratory setup was developed along with the working procedure so that the surface corrosion dynamics of steel could be characterized when droplets of a corrosive medium evaporate from the surface.

The corrosion medium was water with an electrical conductivity and pH close to rainwater, and, for a limited number of water tests, *NaCl* was added.

In order to analyze the experimental evaporation–corrosion data, a complex mathematical model based on simultaneous heat and mass transfer and simultaneous oxygen transfer with surface reaction was considered.

The expression, in the evaporation–corrosion model, of the evaporation surface for the droplet size was solved by integral analysis with respect to the droplet shape.

It has been shown that the evaporation of the drop occurs with the preservation of the original trace and that the rust resulting from corrosion is deposited on this trace.

In the calibration numerical model, values for the basic parameters of the model were identified, i.e., surface reaction rate constant at  $4.5 \times 10^{-5}$  m/s, oxygen diffusion coefficient through the rust layer at  $9.1 \times 10^{-10}$  m<sup>2</sup>/s, *m* constant from the Equation (21) to 0.33, respectively, and  $\alpha$  from Equation (24) to  $2.63 \times 10^{-4}$  m<sup>2</sup>·s (Table 9). When *NaCl* was present in the corrosion medium, at the concentration level of 1 g/L, the surface reaction rate constant increased 21 times. The same increase was identified for the oxygen diffusion coefficient through the crust.

For all 30 evaporation–corrosion tests, reported in Table 10, a good, even very good, coverage of the experimental results of droplet evaporation and corrosion dynamics was sustained qualitatively by graphic representations from Figures 14–17 and quantitatively by identification of an acceptable range for the mean relative deviation experiment model ( $\epsilon_{mpM}$  and  $\epsilon_{mruM}$ , respectively).

Excellent model–experiment agreement was obtained regarding the dynamics of the rust mass associated with a droplet.

In the case of evaporation-droplet corrosion with *NaCl* content, the involvement of *Cl*<sup>-</sup> ions in the anodic corrosion process, led to a strong change in the reaction rate constant and the oxygen diffusion coefficient through the rust layer values, so that we could obtain, for the dynamics of the mass deposited by the rust, a good agreement between the model and the experiment.

It was shown that the developed model can be adapted so that they can serve to simulate surface corrosion when on the droplets have an accepted size distribution or when natural convection is replaced by forced convection.

**Author Contributions:** Conceptualization, M.C.I., T.D. and C.E.R.; methodology, M.C.I. and T.D.; validation, T.D., O.C.P., I.M., T.V.C. and I.M.D.; formal analysis, T.D., O.C.P., I.M., T.V.C. and I.M.D.; investigation, M.C.I. and T.D.; data curation, M.C.I., T.D. and C.E.R.; writing—original draft preparation, T.D. and M.C.I.; writing—review and editing, O.C.P. and C.E.R.; supervision, T.D. All authors have read and agreed to the published version of the manuscript.

**Funding:** This work has been funded by the European Social Fund from the Sectoral Operational Programme Human Capital 2014–2020, through the Financial Agreement with the title “Training of PhD students and postdoctoral researchers in order to acquire applied research skills—SMART”, Contract no. 13530/16.06.2022—SMIS code: 153734.

**Institutional Review Board Statement:** Not applicable.

**Informed Consent Statement:** Not applicable.

**Data Availability Statement:** Not applicable.

**Conflicts of Interest:** The authors declare no conflict of interest.

## References

1. Gerhardus, K.H.; Michel, B.H.P.; Neil, T.G.; Virmani, P.Y.; Payer, J.H. Corrosion Costs and Preventives Strategies in the United States. Available online: <https://impact.nace.org/documents/ccsupp.pdf> (accessed on 3 August 2023).
2. Ke, W.; Li, Z. Survey of Corrosion Cost in China and Preventive Strategies. *Corros. Sci. Technol.* **2008**, *7*, 259–264.

3. Chico, B.; Fuente, D.; Díaz, J.; Simancas, J.; Morcillo, M. Annual Atmospheric Corrosion of Carbon Steel Worldwide. An Integration of ISOCORRAG, ICP/UNECE and MICAT Databases. *Materials* **2017**, *10*, 601. [[CrossRef](#)] [[PubMed](#)]
4. Hou, W.; Liang, C. Atmospheric corrosion prediction of steels. *Corrosion* **2004**, *60*, 313–322. [[CrossRef](#)]
5. Díaz, I.; Cano, H.; Chico, B.; De la Fuente, D.; Morcillo, M. Some clarifications regarding literature on atmospheric corrosion of weathering steels. *Int. J. Corros.* **2012**, *2012*, 812192. [[CrossRef](#)]
6. Forolius, A.Z. The Kinetics of Anodic Dissolution of Iron in High Purity Water. *Corros. Eng.* **1979**, *28*, 10–17. [[CrossRef](#)] [[PubMed](#)]
7. Klinessmith, D.E.; McCuen, R.; Albrecht, H.P. Effect of environmental conditions on corrosion rates. *J. Mater. Civil. Eng.* **2007**, *19*, 121–129. [[CrossRef](#)]
8. Morcillo, M.; Chico, B.; Díaz, I.; Cano, H.; De la Fuente, D. Atmospheric corrosion data of weathering steels. A review. *Corros. Sci.* **2013**, *77*, 6–24. [[CrossRef](#)]
9. To, D. Evaluation of Atmospheric Corrosion in Steels for Corrosion Mapping in Asia, Chapter 2. Ph.D. Thesis, Graduate School of Engineering, Yokohama National University, Yokohama, Japan, 2017.
10. Ilie, M.C.; Maior, I.; Raducanu, C.E.; Deleanu, I.M.; Dobre, T.; Parvulescu, O.C. Experimental Investigation and Modeling of Film Flow Corrosion. *Metals* **2023**, *13*, 1425. [[CrossRef](#)]
11. Tsuru, T.; Tamiya, K.I.; Nishikata, A. Formation and growth of microdroplets during the initial stage of atmospheric corrosion. *Electrochim. Acta* **2004**, *49*, 2709–2715. [[CrossRef](#)]
12. Sainz-Rosales, A.; Ocampo-Lazcarro, X.; Hernández-Pérez, A.; González-Gutiérrez, A.G.; Larios-Durán, R.E.; Ponce de León, C.; Walsh, C.F.; Bárcena-Soto, M.; Casillas, N. Classic Evans's Drop Corrosion Experiment Investigated in Terms of a Tertiary Current and Potential Distribution. *Corros. Mater. Degrad.* **2022**, *3*, 270–280. [[CrossRef](#)]
13. Narhe, R.D.; González-Vinas, W.; Beysens, D.A. Water condensation on zinc surfaces treated by chemical bath deposition. *Appl. Surf. Sci.* **2010**, *256*, 4930–4933. [[CrossRef](#)]
14. Lawrence, G.M. The relationship between relative humidity and the dewpoint temperature in moist air: A simple conversion and applications. *Bull. Am. Meteorol. Soc.* **2005**, *86*, 225–233. [[CrossRef](#)]
15. Evans, U.R. Mechanism of rusting. *Corros. Sci.* **1969**, *9*, 813–821. [[CrossRef](#)]
16. Chen, C.; Mansfeld, F. Potential distribution in the Evans drop experiment. *Corros. Sci.* **1997**, *39*, 409–413. [[CrossRef](#)]
17. Venkatraman, M.S.; Cole, I.S.; Gunasegaram, D.R.; Emmanuel, B. Modelling Corrosion of a Metal under an Aerosol Droplet. *Mater. Sci. Forum* **2010**, *654–656*, 1650–1653. [[CrossRef](#)]
18. Tejaswi, J.; Wang, Z.; Askounis, A.; Orejon, D.; Harish, S.; Takata, Y.; Mahapatra, P.S.; Pattamatta, A. Evaporation kinetics of pure water drops: Thermal patterns, Marangoni flow, and interfacial temperature difference. *Phys. Rev. E* **2018**, *98*, 052804.
19. Hua, H.; Larson, R.G. Marangoni Effect Reverses Coffee-Ring Depositions. *J. Phys. Chem. B* **2006**, *110*, 7090–7096. [[CrossRef](#)]
20. Yuri, O.P. Evaporative deposition patterns: Spatial dimensions of the deposit. *Phys. Rev. E* **2005**, *71*, 036313.
21. Somlyai-Sipos, L.; Baumli, P. Wettability of Metals by Water. *Metals* **2022**, *12*, 1274. [[CrossRef](#)]
22. Xu, J.; Li, B.; Lian, J.; Ni, J.; Xiao, J. Wetting behaviors of water droplet on rough metal substrates. *Adv. Eng. Res.* **2016**, *9*, 341–345.
23. Dobre, T.; Pârvulescu, O.C.; Stoica-Guzun, A.; Stroescu, M.; Jipa, I.; Al Janabi, A.A. Heat and mass transfer in fixed bed drying of non-deformable porous particles. *Int. J. Heat Mass Transf.* **2016**, *103*, 478–485. [[CrossRef](#)]
24. Dobre, T.; Zicman, L.R.; Pârvulescu, O.C.; Neacșu, E.; Ciobanu, C.; Drăgolici, F.N. Species removal from aqueous radioactive waste by deep-bed filtration. *Environ. Pollut.* **2018**, *241*, 303–310. [[CrossRef](#)] [[PubMed](#)]
25. Duda, I.; Gradinaru, S. Calculation of areas in parametric coordinates. In *Integral Calculus with Applications*; Romania of Tomorrow Publishing House: Bucharest, Romania, 2007; pp. 394–452. ISBN 978-973-725-824-3.
26. Xiongjiang, Y.; Jinliang, X. Does sunlight always accelerate water droplet evaporation? *Appl. Phys. Lett.* **2020**, *116*, 253903.
27. Van Gaalen, R.T.; Diddens, C.; Wijshoff, H.M.A.; Kuerten, J.G.M. Marangoni circulation in evaporating droplets in the presence of soluble surfactants. *J. Colloid Interface Sci.* **2021**, *584*, 622–633. [[CrossRef](#)] [[PubMed](#)]
28. Girard, F.; Antoni, M.; Sefiane, K. On the effect of Marangoni flow on evaporation rates of heated water drops. *Langmuir* **2008**, *24*, 9207–9210.
29. Perry, H.D.; Green, W.D.; Malloney, O.J. *Perry's Chemical Engineering Handbook*, 7th ed.; McGraw—Hill: San Francisco, CA, USA, 1997; pp. 78–80.
30. Steeman, H.J.; Janssens, A.; De Paepe, M. On the applicability of the heat and mass transfer analogy in indoor air flows. *Int. J. Heat Mass Transf.* **2009**, *52*, 1431–1442. [[CrossRef](#)]
31. Bird, B.R.; Stewart, E.W.; Lightfoot, N.E. *Transport Phenomena*, 2nd ed.; John Wiley & Sons: Hoboken, NJ, USA, 2002; pp. 442–443.
32. Leca, A.; Pop, M.G.; Prisecaru, I.; Neaga, C.; Zidaru, G.H.; Musatescu, V.; Isbasoiu, E.C. *Calculation Guide. Tables, Nomograms and Thermotechnical Formulas*; Technical Publishing House: Bucharest, Romania, 1987; Volume 2, p. 71.
33. Davies, J.T.; Rideal, E.K. Chapter: Mass Transfer across Interfaces. In *Interfacial Phenomena*; Academic Press: New York, NY, USA, 1963.
34. Dobre, T.; Stoica, A. *Mass Transfer Intensification*; Electra Publishing House: Florence, Italy, 2017; Chapter 7.
35. Ahmed, S.; Hou, Y.; Lepkova, K.; Pojtanabuntoeng, T. Investigation of the effect chloride ions on carbon steel in closed environments at different temperatures. *Corros. Mater. Degrad.* **2023**, *4*, 364–381. [[CrossRef](#)]
36. Morcillo, M.; Chico, B.; Alcantara, J.; Diaz, I.; Simancas, J.; De la Fuente, D. Atmospheric corrosion of mild steel in chloride-rich environments. Questions to be answered. *Mater. Corros.* **2015**, *66*, 882–892. [[CrossRef](#)]

---

**Disclaimer/Publisher's Note:** The statements, opinions and data contained in all publications are solely those of the individual author(s) and contributor(s) and not of MDPI and/or the editor(s). MDPI and/or the editor(s) disclaim responsibility for any injury to people or property resulting from any ideas, methods, instructions or products referred to in the content.